Published in final edited form as:
Magn Reson Med. 1997 January ; 37(1): 124–130.

Techniques for High-speed Cardiac Magnetic Resonance Imaging in Rats and Rabbits

Wolfgang G. Rehwald, **Scott B. Reeder**, **Elliot R. McVeigh**, and **Robert M. Judd**

From the Departments of Radiology (W.G.H., E.R.M., R.M.J.) and Biomedical Engineering (S.B.R., E.R.M.). The Johns Hopkins Medical Institutions, Baltimore, Maryland.

Abstract

Progress in research on hypertension, heart failure, aging, post-infarct remodeling, and the molecular basis of cardiovascular diseases in general has been greatly facilitated in recent years by the development of specialized small-mammal models by selective breeding and/or genetic alteration. Routine noninvasive evaluation of cardiac function and perfusion in these animals models, however, is difficult using existing methods. In principle, MRI can be used for this purpose, but in practice this is difficult because of problems related to RF coils, cardiac gating, and imaging pulse sequences. In this article, solutions to these problems are described that have allowed us to use MRI to routinely image the hearts of rats and rabbits. Specifically described are four RF coils, cardiac gating schemes, and an imaging pulse sequence specially designed for cardiac imaging in these animals on a 4.7 T Omega chemical-shift imaging (CSI) spectrometer. These techniques can be used to obtain, within 2 min, eight double-oblique short-axis images of the rat at different cardiac phases with 200 × 400 μm in-plane resolution and a slice thickness of 2 mm. Moreover, myocardial tissue tagging can be performed with tag thicknesses and separations comparable to those used routinely in humans. The technical information is presented in sufficient detail to allow researchers at other sites to reproduce the results. This information should facilitate the use of MRI for the noninvasive examination of cardiac function and perfusion, which can be combined with other established techniques for the study of cardiovascular disease in specialized animal models.

Keywords

MRI; rat; rabbit; RF coils

INTRODUCTION

Historically, much of our knowledge of cardiac and cardiovascular physiology has been obtained through the use of animal models. At present, rats, rabbits, and dogs are among the most commonly used species in cardiovascular research. Because, at least in part, of the much higher costs associated with large animal models, the use of dogs in cardiovascular research has declined in recent years. On the other hand, the study of smaller animals such as rats and rabbits has been facilitated by the development of specialized animal models of various cardiac and cardiovascular diseases. For example, spontaneously hypertensive rats (SHR) and their genetically identical controls (Wistar-Kyoto [WKY]) are routinely used in hypertension research (1). Similarly, established rat and/or rabbit models of heart failure (2,3), aging (4,5), and postinfarct remodelling (6) have been developed and extensively studied. The utility of

Address correspondence to: Robert M. Judd, Ph.D., Feinberg Cardiovascular Research Institute, Tarry 12-703, Northwestern University Medical School, 303 East Chicago Avenue, Chicago, IL 60611-3008..

these animal models is exemplified by the development of angiotensin-converting enzyme inhibitors (ACEI) (2), which are now in widespread clinical use. In addition, small mammals are central to research in the molecular aspects of cardiovascular disease (7-9). Thus, the success of future research into many aspects of cardiac and cardiovascular disease depends critically on the ability to study small animal models.

A noninvasive method to routinely examine cardiovascular function during disease progression would represent a powerful tool allowing the investigator to perform repeated analyses of a single group of animals, rather than analyses of multiple experimental groups with sacrifice of the animals at different time points. Furthermore, whereas current experimental designs are typically limited to *in vitro* examination, a noninvasive method would allow the investigator to observe the *in vivo* consequences of pathophysiologic processes (9). In this article, we focus on the use of MRI, which allows the examination of multiple parameters such as function and perfusion using a single procedure, for this specific purpose.

Almost 10 years ago, Hedlund *et al*. (10,11) showed that MR "microscopy" techniques could be used to acquire multislice cardiac images of the rat with voxel sizes on the order of 200 × 200 μm and 2.5-mm–thick slices using a whole-body 1.5T magnet. Unfortunately, however, image acquisition times were 30 min or more (10,11). Since that time, many practical improvements have been described, including the use of high-speed gradient-echo imaging techniques (12), segmented *k*-space data acquisition (13,14), echo-planar imaging (15,16), the use of high-field (e.g., 4.7T) magnets to increase image signal-to-noise ratio (SNR) (12), and RF coils specifically designed for cardiac imaging in small animals (15-17).

To be a truly useful tool for the study of cardiovascular physiology, virtually all of the above techniques must be combined to allow routine acquisition of high-speed, high-resolution images of the heart. In this article, we describe how we modified the hardware and software on our 4.7T Omega CSI Spectrometer (General Electric/Bruker, Billerica, MA) to allow study of cardiac and cardiovascular disorders (9). Using these techniques, we can acquire, for example, double-oblique short axis images of rat hearts at eight cardiac phases with 200 × 400 μm in-plane resolution and a 2-mm–thick slice in a total of 2 min, with or without tissue tagging. The purpose of this study is to provide enough technical detail about RF coils, cardiac gating, and pulse sequences to allow other researchers to replicate our techniques. This information should facilitate the use of MRI for the *in vivo* examination of cardiac function and perfusion in specialized animal models of cardiovascular disease.

METHODS

Cardiac imaging of rats and rabbits on a 4.7T Omega CSI spectrometer required specialized RF coils, efficient gating techniques, and a specialized pulse sequence. Each of these are separately described.

RF COILS

Four RF coils are described: 1) a Helmholtz rat coil, 2) a cosine rat coil, 3) a Helmholtz rabbit coil, and 4) a cosine rabbit coil. Because the general characteristics of Helmholtz and cosine RF coil design are well known (18), we describe only those characteristics specific to the design of these coils for rats and rabbits at 200 MHz (^{1}H at 4.7T). Each of the four coils was constructed, tested for homogeneity and SNR, and evaluated for *in vivo* imaging.

Because the filling factor of an RF coil should be maximized for optimal-image SNR (18), the dimensions of the animal to be studied should be carefully considered. Accordingly, we measured the physical dimensions of both rats and rabbits, and the results are summarized in Table 1. In general, we found that the shorter the coil the more its diameter can be decreased

while still allowing adequate placement and positioning, whereas a longer coil has to be considerably bigger in diameter to enable breathing of the animal and to allow it to be placed inside the tube. In addition, we found that rats can grow from a body weight of 210 g to 370 g over the 4-week period typically used to study cardiovascular issues such as postinfarct remodeling. Tables 2 and 3 summarize the length and diameters of the RF coils constructed, which we believe result in the largest practical filling factors.

Helmholtz Coil for Rats and Rabbits—Figure 1 shows schematically the design of both the rat and rabbit Helmholtz coils. Table 2 gives the exact dimensions of each of these coils with regard to Fig. 1. The same electrical design was used for both the rat and rabbit coils. The two halves of the Helmholtz pair were connected in series to assure that the same current passes the two loops, thus improving homogeneity. The connections to and from the two loops run parallel to each other and are insulated by a 0.2-mm–thick mylar sheet. The currents in this connection to the tuning circuit are equal in magnitude but opposite in sign and approximately cancel. Thus, only the current in the two loops contributes to the magnetic field. In addition, four (rat) or eight capacitors (rabbit) were distributed evenly over the coil (see Table 3 for capacitor values). These capacitors increase the resonant frequency to the desired 200 Mhz and also serve to reduce dielectric losses in the sample and thus improve SNR.

The rat Helmholtz coil is made of 0.5-cm–wide copperfoil mounted on the outer side of a plexiglas tube. This small tube slides in a bigger plexiglas tube with an inner diameter of 5.6 cm. Both tubes can be taken apart, which is necessary to put the rat into the coil. Afterward, the rat with the small tube around its ribcage carrying the actual coil is slid into the bigger tube. The coil is mounted to the bigger tube by screws. The rabbit Helmholtz coil is permanently mounted in a plexiglass half-shell with a diameter slightly smaller than that of our smaller gradient coil set (15 cm, S-150).

Vendors for specific RF coil components are listed in the Appendix.

Rat Cosine Coil—Figure 2a shows the fully assembled rat cosine coil, whereas Figs. 2c and 2d show this coil disassembled for greater detail. The rat cosine coil is bigger in diameter than the rat Helmholtz coil (see Table 3). The bigger diameter was chosen to allow improved precision of the cosine-distributed rods. A conducting aluminum cylinder is used as shielding, which increases the coil's resonant frequency by decreasing the coil's inductance. A fortuitous side effect of using the shielding cylinder is that the resonant frequency does not change when the coil is put into the bore of the MRI magnet, whereas unshielded coils may experience a rise in frequency when the coil is brought into the magnet. Another advantage is that coupling between coil and gradients is reduced. To tune the resonant frequency, two serial capacitors are introduced in the paths to both ends of the cosine coil (see Table 3 for capacitor values).

Rabbit Cosine Coil—The rabbit cosine coil is shown in Fig. 2b. This coil is built in a manner similar to that of the rat cosine coil except with larger dimensions (inner diameter = 12.2 cm. length = 7 cm, Table 3). An aluminum shielding was used to increase the resonance frequency, and tuning capacitors were placed in the connecting paths to the coil (values given in Table 3). The rods are soldered on copper foil end rings mounted on a plexi-glass tube. This construction is then attached to a larger plexiglass tube with an outer diameter of 15 cm and a wall thickness of 3 mm. This diameter is equal to the bore diameter of the small gradient set (S-150) in our spectrometer (15 cm). For both the rat and the rabbit cosine coil, copper rods are used. In both cases, the end rings are made of 1.2-cm–wide copper foil.

SNR and Homogeneity—To evaluate homogeneity and SNR of the four coils, images of phantoms were acquired. For the rat coils, a 4-cm–diameter bottle filled with saline was imaged, whereas a 9-cm–diameter bottle was used for the rabbit coils. A gradient-recalled echo-pulse

sequence (see Imaging Pulse Sequence) was used with $\alpha = 90°$, *TE* = 4.5 (rat) or 3.0 (rabbit) ms, *TR* = 3 s, matrix 256 × 128, number of averages = 2, and field of view (FOV) = 50 (rat) or 150 (rabbit) mm. The long *TR* was chosen to allow nearly full relaxation, and as a consequence total imaging times were 12.8 min (3 × 128 × 2 sec).

In-vivo–image SNR was measured for the four coils using the software package, NIH Image (National Institutes of Health, Bethesda, MD). The mean intensity and the standard deviation within the region of interest (phantom or cardiac muscle) and outside the sample (noise), respectively, were then measured, and SNR was calculated as: mean image intensity in the sample/(l.5 * standard deviation of the noise) (19).

Cardiac Gating and Animal Preparation

Ideally, the *R*-wave of the ECG should be used for cardiac gating. Unfortunately, we found that ECG gating of rats and rabbits is very difficult on our spectrometer for several reasons. First, the amplitude of a rat's ECG appears to be smaller in animals with chronic myocardial infarction, perhaps because of the loss of large numbers of myocytes. Second, typically there is interaction between the spectrometer's gradients and ECG leads such that false triggers during scanning are problematic. Third, and in our case most importantly, the ECG leads act as antennae that directly introduce stray RF noise from the surroundings to the RF coil, resulting in image artifacts. To avoid these problems, we used blood-pressure gating.

After anesthesia with 35 mg/kg sodium pentobarbital, a femoral artery of the rat or rabbit was cannulated. Polyethylene tubing 0.030″ and 0.038″ outer diameter were used as cannulae for rats and rabbits, respectively. Surgical needles were inserted into the polyethylene cannulae and connected to a Statham P23 pressure transducer amplified by a Gould Universal Amplifier (Cleveland, OH). The gain was set at the maximum value (0.05 volts full scale) to ensure a sharp upslope for the triggering circuit logic. The analog signal was processed by the Gould Universal Amplifier with the low-pass filter set at 10 Hz to eliminate fluctuations resulting from respiration, and the high-pass filter was set at a 30-Hz filter to remove noise. The signal was then fed into a gating box supplied with our 4.7T spectrometer. After the experiment, the catheter was removed, the femoral artery was tied off, and the wound was closed. The animals recovered and could be imaged on two other occasions by using the other femoral and a carotid artery for cannulation on subsequent imaging sessions.

The use of pressure gating does not complicate the acquisition of end-systolic and end-diastolic images, because images at multiple cardiac phases are interleaved on acquisition (see Imaging Pulse Sequence) and spaced throughout the entire cardiac cycle. Using this approach, end-systolic and end-diastolic images can be identified within a set of, for example, 8 to 16 images rather than by a acquiring single image at a specified delay after the *R*-wave. Note that the latter approach would require the same total imaging time as for the whole set of 8 or 16 images using interleaved acquisition.

In some rats, chronic myocardial infarction was induced by ligation of a coronary artery. The details of the preparation are given elsewhere (9). Briefly, the hearts were exposed using an intercostal incision, the pericardium was opened, and an anterior branch of the left coronary artery was permanently ligated. The rats were then allowed to recover and studied using MRI at 1 day, 2 weeks, and 4 weeks postinfarct.

For all animals, an oxygen line was placed into the animal's mouth to facilitate respiration by enhancing the oxygen concentration in the inhaled air. Mechanical respiration was not used, and the images were not respiratory gated.

Imaging Pulse Sequence

An ultrafast gradient-echo pulse sequence suitable for cardiac imaging was written for our GE/Bruker 4.7T Omega[1] (20). This cardiac-gated pulse sequence performs ultrafast oblique imaging using the principles of *k*-space segmentation for data acquisition (13,14). The Omega is equipped with 150-mm Accustar S150 gradients, capable of 19.6 G/cm maximum gradient strength and 40 μs/(G/cm) switching time, although we typically used only 20% of these maximum values in our imaging experiments. The fast gradients and several features of the pulse sequence, described below, were important in achieving the goal of high-speed, high-resolution cardiac imaging. Fig. 3 diagrams the pulse sequence.

Unlike most clinical scanners, our Omega system is not equipped with oblique hardware boards, necessitating oblique gradient commands in the pulse sequence. In general, this increases gradient waveform memory by threefold, and often exceeds the maximum waveform memory. Accordingly, half-period sinusoid gradients are used for many of the gradient waveforms. A trapezoidal gradient, for example, requires nine waveforms in oblique coordinates, whereas a half-sine lobe needs only three. Because the slice-selection gradient was chosen as a sine lobe, the RF pulse must be properly mapped in time and amplitude, according to *k*-space excitation theory by Pauly *et al.* (21), to provide the same slice selection achieved with a standard slice selection. A simple sinc waveform used with a trapezoidal gradient can be written as:

$$\text{sinc}\,(t) = B_1 \frac{\sin(\pi t/T)}{\pi t/T} \qquad [1]$$

where B_1 is the amplitude of the pulse at $t = 0$, T is the duration of the trapezoid plateau, and $t = 0$ is the center of the pulse. According to Pauly's theory, the amplitude must be weighted by the velocity through excitation *k*-space. In addition, time must be mapped to deposit energy correctly during its trajectory. It can be shown that the correct RF waveform to use with the half-sine gradient is:

$$sinc\,(t) = B_1 \cos\left(\frac{\pi t}{2T_a}\right) \frac{\sin\left(\frac{\pi}{2}\sin\left(\frac{\pi t}{2T_a}\right)\right)}{\frac{\pi}{2}\sin\left(\frac{\pi t}{2T_a}\right)} \qquad [2]$$

where T_a is the duration of the RF excitation shown in Fig. 3. There are several advantages of using such a pulse, in addition to the reduction of gradient waveforms in oblique coordinates. Because the RF begins to play *immediately*, slice selection time and slice refocussing lobe area are reduced, significantly shortening *TR* and *TE*. First-moment artifacts caused by through-slice motion are also reduced.

Lastly, fractional echo acquisition is used by reducing the area of the readout prephaser lobe. Although there is some loss of SNR with the use of fractional echoes [22], it allows for substantial reductions of *TR* and *TE*. In addition, first-moment velocity artifacts due to in-plane ventricular blood flow are significantly reduced with partial echoes (14). A fractional echo is characterized by ζ, defined as,

$$\zeta = \frac{k_x^{\max} - k_x^{\min}}{2k_x^{\max}} \qquad [3]$$

where $k_x^{\max}$ and $k_x^{\min}$ are the boundaries between which *k*-space is sampled. ζ is 1 for a centered echo and 0.5 for a free-induction decay (FID). We have found that $\zeta = 0.6$ to 0.7 provides a reasonable compromise between a short echo time and loss of information caused by

[1]All details of this pulse sequence are available through anonymous file transfer protocol at tempest.bme-mri.jhu.edu under ~pub/papers/Reeder/.

asymmetric echo formation. Imaging tip angle is nominally set to the Ernst angle, and for tagging it has been shown that tag-tissue contrast is optimized for tip angles between 11 and 15° (23). For a bandwidth of 66 kHz and a FOV of 50 mm, $TR \approx 11–14$ ms and $TE \approx 3–5$ ms are easily achieved.

For rats, the imaging pulse-sequence parameters were: α = Ernst Angle (ca. 15°), TE = 4.5 ms, TR = 12 ms, matrix 256 × 128, number of averages = 8, number of cardiac phases = 8, number of image-encoding steps/cardiac phase/beat = 2, and FOV = 50 mm. The total number of cardiac cycles required for the eight rat images was 512 (number of averages * phase encoding resolution/number of steps per phase per beat = 8 * 128/2), or 1.7 min for a heart rate of 300 beats per minute (BPM). For rabbits, the parameters were: α = Ernst Angle (ca. 15°), TE = 3.0 ms, TR = 7 ms, matrix 256 × 128, number of averages = 16, number of cardiac phases = 8, number of image encoding steps/cardiac phase/beat = 4, and FOV = 150 mm, The total number of cardiac cycles required for the eight rabbit images was also 512 (= 16 * 128/4), or 2.1 min for a heart rate of 240 BPM.

RESULTS

Homogeneity

As expected, Helmholtz coils were only homogeneous in the center area of the coil, whereas the left and right upper and lower parts of the field were inhomogeneous. In practice, these inhomogeneities were not a serious problem, because we were primarily interested in imaging the animal's heart, which is located close to the center of the coil. As a measure of homogeneity, the variations in image intensities for the phantom images were ± 6.4, 10.8, 25.7, and 18.9% of the mean over 90% of the area of the thoracic cavity for the rat Helmholtz, rat cosine, rabbit Helmholtz, and rabbit cosine coils, respectively. The unloaded/loaded Q values for the four coils, defined as frequency divided by width at half height, were 1064/281, 73/53, 545/27, and 38/24 for the rat Helmholtz, rat cosine, rabbit Helmholtz, and rabbit cosine coils, respectively.

In-Vivo imaging

Figure 4 shows *in vivo* images acquired with the four coils. The image of Fig. 4a was acquired with the rat Helmholtz coil and shows a tagged rat image with a grid of 1.5 mm × 1.5 mm. This image was one of eight interleaved cardiac phases with a total image acquisition time for the eight images of 4 min. A large, 1-day-old myocardial infarct is situated in the lower left quadrant of the heart, which can be seen as a region in which the tags lines remain straight in this single image and which is more easily seen in a cine display of the eight cardiac phases. Figure 4b shows the heart of a sham rat during diastole acquired with the rat cosine coil. Figures 4c and 4d show noninfarcted rabbit hearts acquired with the Helmholtz and cosine coil, respectively.

Figure 5 shows eight images acquired during different cardiac phases. The times listed below each image correspond to the time after the pressure-gating pulse that the image was acquired. This animal was subjected to myocardial infarction 2 weeks before imaging. As can be seen clearly, the left and lower parts of the left ventricle are much thinner than the rest of the cardiac muscle. Based on postmortem examination, this thin region comprises fibrosis reflecting the myocardial infarction. The heart is clearly dilated compared with the noninfarcted heart (e.g., Fig. 4b), reflecting progressive heart failure in this animal. This scar region shows no contraction, whereas the remaining viable myocardium exhibits dysfunction, as can be seen by comparing all eight phases. Furthermore, because of the greatly decreased contraction, we found the ejection fraction in this animal was only approximately 20% compared with ca. 80% in normal rats. Images such as those in Fig. 5 demonstrate the potential of MRI in small

mammals to examine noninvasively the pathophysiologic changes that occur after myocardial infarction.

Using the imaging parameters described in the Imaging Pulse Sequence section, we found that the number of pixels across the heart wall were typically 12 in the readout direction and six in the phase-encode direction for both the rat and rabbit images. This compares favorably with currently used techniques to image the human heart clinically (typically 10 pixels across the left ventricular wall). Achieving this in-plane resolution with the available signal, however, required that we use somewhat thicker slices than would be used clinically, however. For example, adequate-image SNR in rats was achieved using a 2-mm slice thickness such that coverage of the entire rat heart required approximately 5 short-axis slices. Clinically, however, perhaps 10 base-apex images would be acquired such that our resolution in the slice direction is approximately two times lower than that typically used in humans.

SNR

For rat myocardium, the *in vivo* SNR for a voxel size of 200 × 400 μm × 2 mm (Fig. 4) was 11 for the Helmholtz coil and 8 for the rat cosine coil. For rabbits, the SNR for a voxel size of 600 × 1200 μm × 3 mm was 27 for the Helmholtz coil and 22 for the cosine coil.

DISCUSSION

We have described techniques by which high-speed, high-resolution images of rats and rabbits can be acquired at 4.7T using spectrometers currently available in research institutions. The technical data of this article should provide sufficient information to allow researchers at other sites to reproduce our results. Using techniques such as these, it should be feasible to combine MRI of rats and rabbits for the noninvasive examination of cardiac function and perfusion *in vivo.* These *in vivo* data can then be combined with established invasive techniques of examining cellular and microvascular changes in the same animals establishing the role of MRI as an important tool for the investigation of fundamental processes in cardiovascular disease.

Acknowledgements

This work was supported by a Biomedical Engineering Research grant from the Whitaker Foundation (R.M.J.) and National Institutes of Health grants NIH-NHLBI R29-HL45683 (E.R.M.) and NIH-NHLBI R29-HL53411 (R.M.J.).

APPENDIX COMPANY ADDRESSES

High-voltage trimmer capacitors can be ordered from: Voltronics Corporation 100-10 Ford Road Denville, NJ 07834 Phone: 201-586-8585 Fax: 201-586-3404

Trimmer capacitors can also be ordered from: Oxley Inc. 25 Business Park Drive P.O. Box 814 Branford, CT 06405 Phone: 203-488-1033 Fax: 488-481-6971

Ceramic capacitors (non magnetic) can be ordered from: American Technical Ceramics One Norden Lane Huntington Station, NY 11746-2102 Phone: 516-547-5700 Fax: 516-547-5748

Copper tape (3M electronic special tape) can be ordered from: Allied Electronics 7410 Pebble Drive Fort Worth, TX 76118 Phone: 800-433-5700 Fax: 410-312-0818

Copper rods and foil can be ordered from: Small Parts Inc. P.O. Box 4650 Miami Lakes, FL 33014-0650 Phone: 305-557-8222 Fax: 800-423-9009

Plexiglas sheets, tubes, mylar, and many other plastics can be ordered from: Gar-Ron Plastics Corporation 5424 Pulaski Highway Baltimore, MD 21205 Phone: 800-492-4695 Fax: 410-483-1493

REFERENCES

1. Kirby RF, Johnson AK. Regulation of sodium and body fluid homeostasis during development: implications for the pathogenesis of hypertension. Experientia 1992;48:345–351. [PubMed: 1582493]
2. Pfeffer JM, Pfeffer MA, Braunwald E. Hemodynamic benefits and prolonged survival with long-term captopril therapy in rats with myocardial infarction and heart failure. Circulation 1987;75:I149–I155. [PubMed: 3539404]
3. Medeiros DM, Davidson J, Jenkins JE. A unified perspective on copper deficiency and cardiomyopathy. Proc Soc Exp Biol Med 1993;203:262–273. [PubMed: 8516340]
4. Caffrey JL, Boluyt MO, Younes A, et al. Aging, cardiac proenkephalin mRNA and enkephalin peptides in the Fisher 344 rat. J. Mol. Cell. Cardiol 1994;26:701–711. [PubMed: 8089851]
5. Xiao R-P, Spurgeon, O'Connor HAF, Lakatta EG. Age-associated changes in beta-adrenergic modulation on rat cardiac excitation-contraction coupling. J. Clin. Invest 1994;94:2051–2059. [PubMed: 7962551]
6. Pfeffer MA, Braunwald E. Ventricular remodeling after myocardial infarction: experimental observations and clinical implications. Circulation 1990;81:1161–1172. [PubMed: 2138525]
7. Sadoshima J, Izumo S. Molecular characterization of angiotensin II-induced hypertrophy of cardiac myocytes and hyperplasia of cardiac fibroblasts: a critical role of the AT1 receptor subtype. Circ. Res 1993;73:413–423. [PubMed: 8348686]
8. Sadoshima J, Qui Z, Morgan JP, Izumo S. Angiotensin II and other hypertrophic stimuli mediated by G protein-coupled receptors activate tyrosine kinase, mitogen-activated protein kinase, and 90-kD S6 kinase in cardiac: myocytes: the critical role of Ca^{+}-dependent signaling. Circ. Res 1995;76:1–15. [PubMed: 8001266]
9. Mellilo G, Lima JAC, Judd RM, Goldschmidt-Clermont PJ, Silverman HS. Intrinsic myocyte dysfunction and tyrosine kinase pathway activation underlie the impaired wall thickening of adjacent regions during post-infarct left ventricular remodeling. Circulation 1996;93:1447–1458. [PubMed: 8641035]
10. Hedlund LW, Johnson GA, Karis JP, Effman EL. MR “microscopy” of the rat thorax. J. Comput. Assist. Tomogr 1986;10:948–952. [PubMed: 3782566]
11. Hedlund LW, Johnson GA, Mills GI. Magnetic resonance microscopy of the rat thorax and abdomen. Invest. Radiol 1986;21:843–846. [PubMed: 3781788]
12. Atkinson DJ, Burstein D, Edelman RR. First-pass cardiac perfusion evaluation with ultrafast MR imaging. Radiology 1990;174:757–762. [PubMed: 2305058]
13. Atkinson DJ, Edelman RR. Cineangiography of the heart in a single breath hold with a segmented turboFLASH sequence. Radiology 1991;178:357–360. [PubMed: 1987592]
14. McVeigh ER, Atalar E. Cardiac tagging with breath-hold cine MRI. Magn. Reson. Med 1992;28:318–327. [PubMed: 1461130]
15. Wendland MF, Saeed M, Ku KY, et al. Inversion recovery EPI of bolus transit in rat myocardium using intravascular and extravascular gadolinium-based contrast media: Dose effects on peak signal enhancement. Magn. Reson. Med 1994;32:319–329. [PubMed: 7984064]
16. Saeed M, Wendland MF, Masui T, Higgins CB. Reperfused myocardial infarctions on T1- and susceptibility-enhanced MRI: evidence for loss of compartmentalization of contrast media. Magn. Reson. Med 1994;31:31–39. [PubMed: 8121266]
17. Sievers RE, Schmiedl U, Wolfe CL, et al. A model of acute regional ischemia and reperfusion in the rat. Magn. Res. Med 1989;10:172–181.
18. Hayes, CE.; Edelstein, WA.; Schenck, JF. Radio frequency resonators. In: Partain, CL.; Price, RR.; Patton, JA.; Kulkarni, MV.; James, AE., Jr., editors. Magetic Resonance Imaging. W. B. Saunders Co.; Philadelphia: 1988. p. 1183-1200.
19. Henkelman RM. Measurement of signal intensities in the presence of noise in MR images. Med. Phys 1984;12:232–233. [PubMed: 4000083]
20. Reeder, SB. Development of High-speed, High-Resolution Magnetic Resonance Imaging and Tagging Techniques. Johns Hopkins University; Baltimore: 1993. Master's Thesis
21. Pauly J, Nisbimura D, Macovski A. A *k*-space analysis of small-tip-angle excitation. J. Magn. Reson 1989;81:43–56.

22. McVeigh, E.; Atalar, RE. The Physics of MRI. American Association of Physicists in Medicine; New York: 1993. Balancing contrast, resolution, and the signal-to-noise ratio.

23. Reeder SB, McVeigh ER. Tag contrast in breath-hold CINE cardiac MRI. Magn. Reson. Med 1994;31:521–525. [PubMed: 8015405]

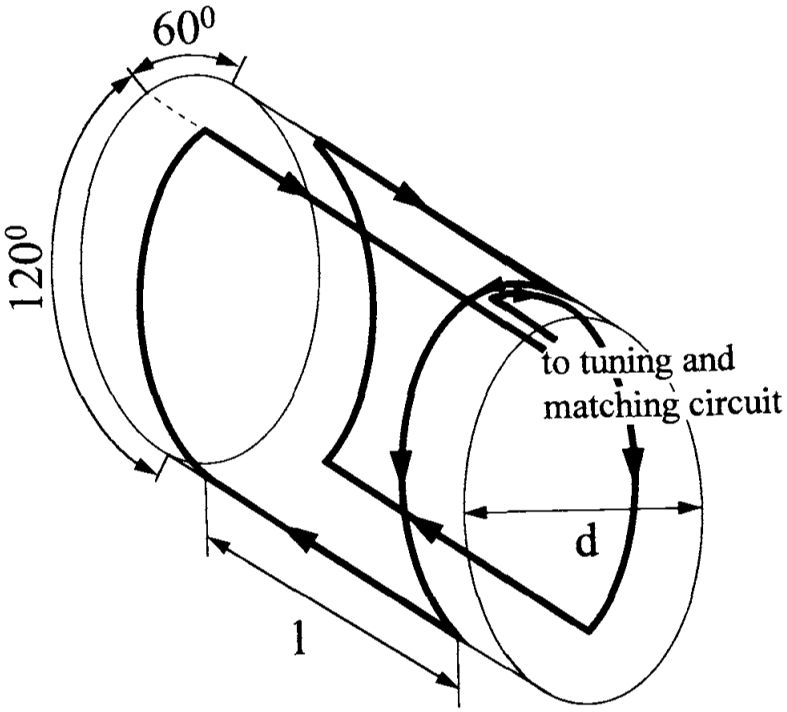

FIG. 1.
Schematic drawing of the Helmholtz coil used for rats and rabbits. The left and right current loop are connected in series. The currents passing through the upper front parallel wires are equal in magnitude but opposite in sign. Dimensions are listed in Table 3.

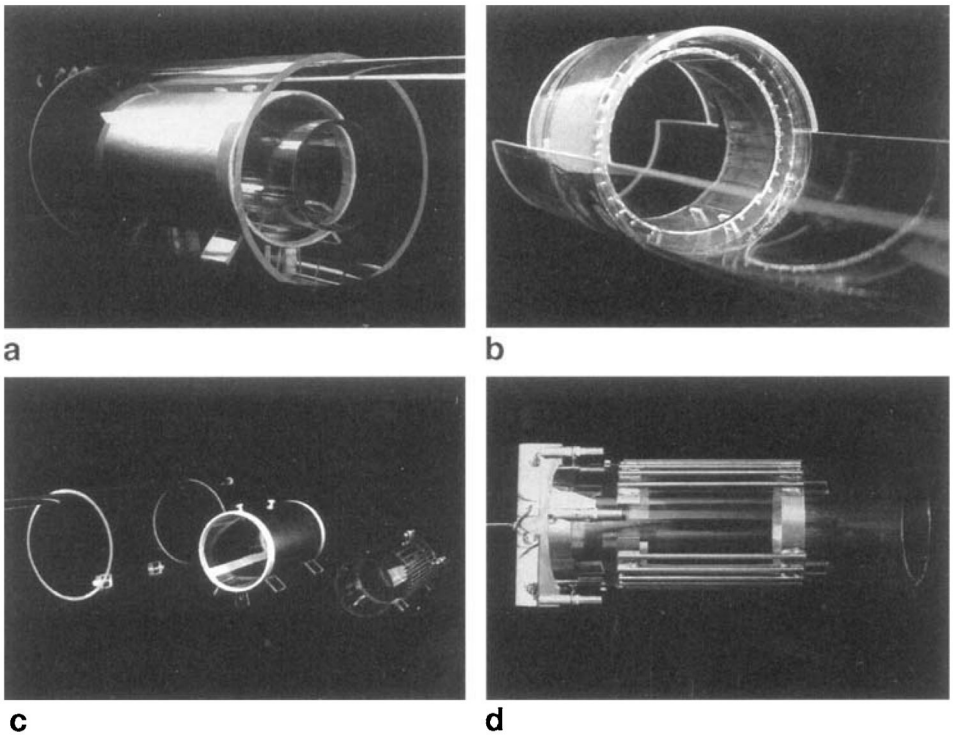

FIG. 2.
Photograph of the cosine coils: (a) assembled rat cosine coil, (b) assembled rabbit cosine coil, (c) exploded view of rat cosine coil, (d) rat cosine coil without shielding and without shell.

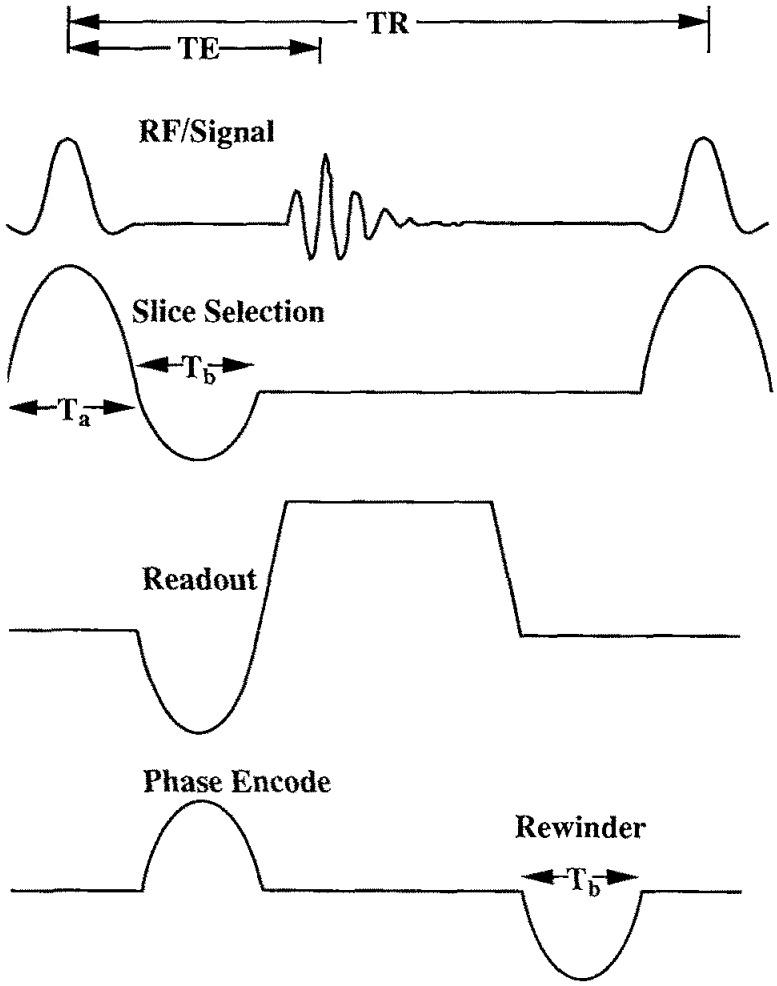

FIG. 3.

Ultrafast cardiac-gated double-oblique gradient-echo pulse sequence written for use on a GE/Bruker 4.7T Omega. Features of this sequence include a sine slice-select gradient lobe, fractional echo, and readout sampling times adjustable to 1-μs precision. Minimum *TR* was approximately 13 ms and *TE* 4.5 ms, for typical rat-imaging parameters.

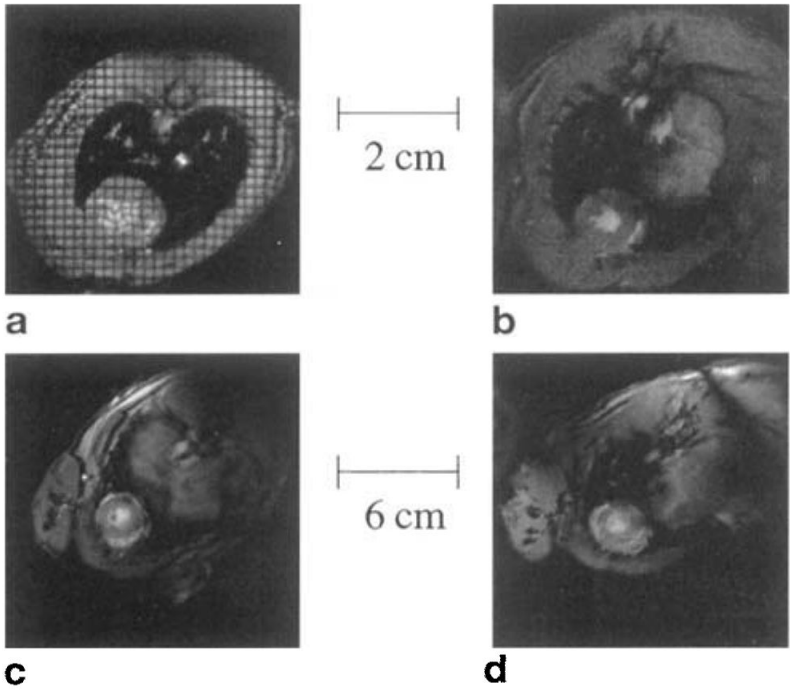

FIG. 4.

MRIs of the heart acquired with four coils. (a) Helmholtz rat coil, (b) cosine rat coil, (c) Helmholtz rabbit coil, (d) cosine rabbit coil. Only the rat Helmholtz image is tagged. The infarction is located on the lower left side of image (a). The other three images are taken from sham animals and hence do not show any infarct.

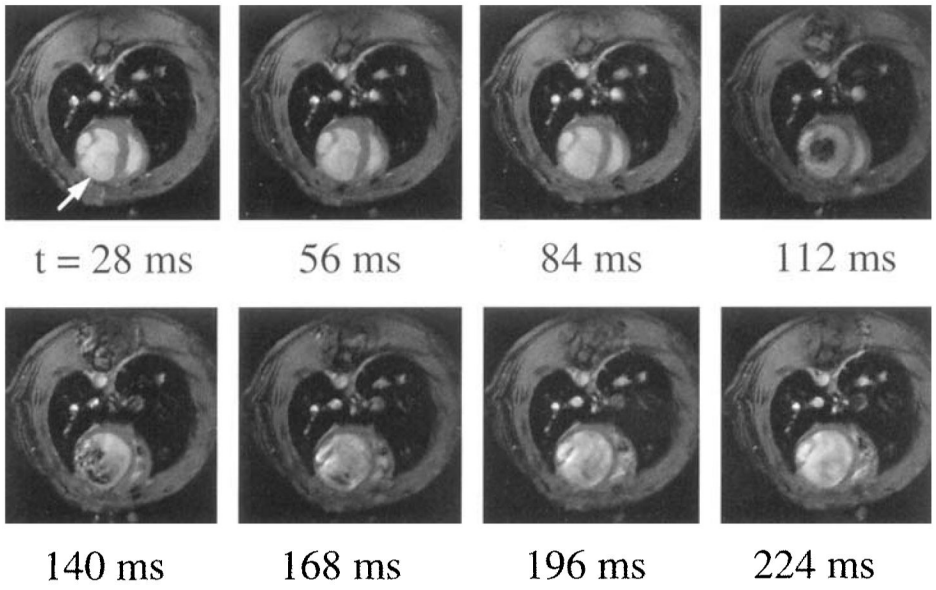

FIG. 5.

Eight phases of the cardiac cycle, acquired at equidistant time points (every 28 ms). Time increases from left to right, then top to bottom. A large infarcted area with highly reduced wall thickness can be seen on the left and lower side of the left ventricle.

Table 1

Physical Dimensions of Animals and RF Coil Design Criteria

Animal	**Rat**	**Rat**	**Rabbit**
Weight	210 g	370 g	5 kg
Diameter of ribcage	1.9 cm	2.5 cm	5.4 cm
Length of ribcage	4 cm	5 cm	11 cm
Length of body w/o tail	18 cm	22 cm	37 cm
Heart's long axis	1.5 cm	2 cm	3 cm
Heart rate (anesthetized animal)	300 bpm	300 bpm	240 bpm
Voxel size	0.2 × 0.4 × 2	0.2 × 0.4 × 2	0.6 × 1.2 × 3
Field of view	50 mm	50 mm	150 mm

Table 2

Length and Diameter of Helmholtz Coils

Coil	Rat	Rabbit
Length	5 cm	11 cm
Diameter	5.1 cm	13 cm

Table 3

Technical Data

Type of coil	Rat Helmholtz	Rabbit Helmholtz	Rat cosine	Rabbit cosine
Outer diameter of tube (diameter of coil)	5 cm	12.8 cm	7 cm	12.8 cm
Inner diameter of tube	4.5 cm	12.2	6.4 cm	12.2 cm
Length of coil	5 cm	11 cm	10.5 cm	7 cm
Diameter of half shell	15.24 cm (6″)	15.24 cm (6″)	15.24 cm (6″)	15.24 cm (6″)
Diameter of shielding			10.3 cm	14.3 cm
Shielding yes/no	No	No	Yes	Yes
Conductors	Copper foil	Copper foil	Copper rods and copper foil	Copper rods and copper foil
Range of tuning/matching capacitors	2 pF–29 pF	2 pF–29 pF	2 pF–29 pF	2 pF–29 pF
Number and value of distributed	4 of 12.2 pF each	4 of 8.2 pF, 4 of about 24 pF		
Width of copper tape	0.5 cm	1.2 cm	1.2 cm (endring)	1.2 cm (endring)
Angles of tape placement	30°, 150°, 210°, 330°	30°, 150°, 210°, 330°		
Number of rods	—	—	26	26
Number and value of serial capacitors	—	—	2 of 16 pF each	2 of 7.5 pF each